(Manuscript #7609R1-Correction, correction date: January 7, 2021)

Incorporation of incompatible trace elements into molybdenite: Layered PbS precipitates within molybdenite

YIPING YANG[1,2,3], HONGPING HE[1,2,3], WEI TAN[1,2*], QI TAO[1,2], JUNMING YAO[1,2], HAIYANG XIAN[1,2], SHANGYING LI[1,2], JIAXIN XI[1,2,3], JIANXI ZHU[1,2,3], HUIFANG XU[4]

[1] *CAS Key Laboratory of Mineralogy and Metallogeny/ Guangdong Provincial Key Laboratory of Mineral Physics and Materials, Guangzhou Institute of Geochemistry, Chinese Academy of Sciences, Guangzhou 510640, China*

[2] *CAS Center for Excellence in Deep Earth Science, Guangzhou, 510640, China*

[3] *University of Chinese Academy of Sciences, Beijing 100049, China*

[4] *Department of Geoscience, University of Wisconsin-Madison, 1215 West Dayton Street, Madison, Wisconsin 53706, U.S.A.*

*Correspondence to: W. Tan (tanwei@gig.ac.cn)

ABSTRACT

Trace elements in molybdenite can provide important information regarding the composition of ore-forming fluid and the evolution and genesis of ore deposits. However, the occurrence states and behavior of relatively incompatible trace elements (e.g., Pb and Os) in natural molybdenite remain ambiguous. Here, we report an abnormally high enrichment of Pb and layered PbS precipitate within molybdenite grains from the Huanglongpu carbonatite-hosted Mo-Pb deposit in the Qinling orogenic belt of Northern China. High-resolution transmission electron microscopy (HRTEM) and related nano-beam techniques were applied to characterize the occurrence states of Pb within molybdenite at the atomic scale. The results show that up to several weight percent of Pb can be incorporated into the molybdenite structure during initial crystallization, which can lead to the formation of screw dislocations and 3*R*/disordered stacking of S-Mo-S sandwich layers. Observations using a scanning transmission electron microscope also reveal that Pb diffuses from the host molybdenite into the layered PbS precipitates under prolonged electron beam irradiation. Pb-bearing molybdenite tends to transform into a Pb-poor ordered $2H_1$ polytype upon Pb exsolution during cooling. Pb preferentially exsolves along the (001) plane of molybdenite and is stored in structural defects (e.g., dislocation loops) and grain boundaries, resulting in nano-scale Pb heterogeneities in molybdenite. Further coarsening of the exsolved Pb results in the formation of layered PbS precipitates along the (001) plane of molybdenite. This study provides an example of the consequences of the incorporation and exsolution of incompatible trace elements in molybdenite and demonstrates that careful mineralogical examination is required to interpret geochemical data obtained by in-situ analysis techniques.

Keywords: Molybdenite, layered PbS, polytype, incompatible trace elements

INTRODUCTION

Molybdenite (MoS_2) is a layered-structure sulfide mineral with two hexagonally coordinated S layers and one sandwiched Mo layer. The sandwich-like [S-Mo-S] layers that stack along the *c*-axis are weakly bonded by van der Waals forces. Molybdenite hosts important economic resources of Mo and Re (Fleischer 1959; Frondel and Wickman 1970; Terada et al. 1971; Plotinskaya et al. 2018). ^{187}Re-^{187}Os systematics in molybdenite are also widely applied to date geological events (Stein et al. 2001, 2003), and trace element (e.g., Pb, Bi, Re, and W) characteristics provide important insight into the multi-stage mineralization history of related deposits (Ciobanu et al. 2013; Barra et al. 2017).

Highly compatible trace elements (e.g., Re and W) are preferentially incorporated into the molybdenite structure due to their same valence and similar ionic radii (e.g., Re^{4+}, 0.63 Å; W^{4+}, 0.66 Å) as Mo^{4+} (0.65 Å), and are commonly considered to be relatively immobile (Stein et al. 2003). In contrast, relatively incompatible trace elements (e.g., Pb, Bi, Te, and Au) commonly occur as independent mineral phases in molybdenite (Petruk 1965; Ciobanu et al. 2013; Pasava et al. 2016; Plotinskaya et al. 2018), have relatively higher mobilities (Stein et al. 2003), and tend to form atomic clusters within structural defects and mm- to nm-sized exsolution/inclusion phases (Stein et al. 2003; Pasava et al. 2016).

An understanding of the mobility of relatively incompatible trace elements in molybdenite is critical to accurately interpreting the trace element data and retrieved isotopic ages. Previous studies have demonstrated the effectiveness of using transmission electron microscopy (TEM) to observe the behavior (e.g., occupancy and migration) of Au and Re in synthetic MoS_2 under electron beam irradiation (Lin et al.

2014a, 2014b). However, the occurrence states and mobility of relatively incompatible trace elements in molybdenite with regards to different geological conditions have received scarce attention in the literature (Stein et al. 2003). The incorporation of trace elements may also influence the formation of polytypes (e.g., 3*R* and $2H_1$) in molybdenite by introducing lattice strain and screw dislocations in the stacked S-Mo-S sandwich layers (Newberry 1979a, 1979b); nevertheless, the relationship between incorporated trace elements and the formation of specific polytypes remains ambiguous (Frondel and Wickman 1970; McCandless et al. 1993; Newberry 1979a, 1979b; Voudouris et al. 2009; Grabezhev and Voudouris 2014; Plotinskaya et al. 2019).

Although relatively incompatible, Pb commonly occurs in relatively high concentrations (ppm to wt.% levels) in molybdenite (Stein et al. 1997; Du et al. 2004; Ciobanu et al. 2013; Pasava et al. 2016), which makes it an ideal candidate for investigating the behavior of relatively incompatible trace elements. In this study, high-resolution transmission electron microscopy (HRTEM) is used with a combination of nanobeam techniques to investigate the occurrence of Pb in molybdenite from the Huanglongpu Mo-Pb ore deposit. The results provide important insight into the behavior of Pb in molybdenite and the correlation between specific polytypes and incompatible trace elements. These findings also provide critical clues for interpreting the uncertainty and anomaly of geochemical data obtained by in-situ analysis techniques.

SAMPLING AND ANALYTICAL METHODS

Sampling

The Qinling orogenic belt is an important Mo mineralization area in China with most Mo contained within the porphyry systems associated with Late Mesozoic granite (Li and Pirajno 2017). Mo mineralization is particularly notable in the Huanglongpu Mo-Pb deposit located in the eastern Qinling orogen belt, which is genetically related to Early Mesozoic carbonatite dykes and mantle-derived elemental resources including Mo, Pb, C, O, and S (Huang et al. 1985; Stein et al. 1997; Xu et al. 2009; Song et al. 2015, 2016; Li and Pirajno 2017). The carbonatite veins consist of 40–60 vol.% calcite, 30–50 vol.% quartz, ~5 vol.% microcline, ~4.5 vol.% barytocelestine, ~1 vol.% biotite, and significant quantities of molybdenite, galena, and pyrite (Stein et al. 1997).

Six molybdenite-bearing specimens were collected from the carbonatite veins in the Huanglongpu Mo-Pb deposit in mostly calcite aggregates (Figs. 1a, 1b). The samples contain two distinct molybdenite occurrences: (1) sparsely disseminated and speckled in the calcite and quartz (Fig. S1a) and (2) densely disseminated and distributed in small strips in the calcite aggregates (Fig. S1b). The samples from the carbonatite veins occur as aggregates of thin flakes ranging from 50 to 80 μm in length and less than 10 μm in thickness (Fig. 1b). Molybdenite has been shown to contain 1–3 wt. % Pb (Stein et al. 1997; Du et al. 2004). Two occurrences of Pb were identified in the studied samples including sub-micro-scale galena filling in the interstitial space of molybdenite clusters (Fig. 1c) and nanoscale layered PbS with an epitaxial relationship with the molybdenite host (Fig. 1d).

Electron microprobe analysis

The chemical composition of the Pb-bearing molybdenite samples was determined using a JEOL JXA-8230 electron probe microanalyzer (EPMA) under the

operating conditions of 20-kV accelerating voltage and 50-nA probe current using a 1-μm beam. The counting times were 20 s for Mo, S, and Fe, 40 s for Ca and Cu, and 60 s for Re, Pb, Zr, As, and W. The analytical lines were ReM_α, WM_α, PbL_α, MoL_α, ZrL_α, AsL_α, CaK_α, FeK_α, CuK_α, and SK_α. The standards for calibration included MoS_2 (Mo, S), rhenium (Re), copper (Cu), and tungsten (W) metals, galena (Pb), pyrite (Fe), zircon (Zr), Cr-diopside (Ca), and arsenopyrite (As).

Micro-X-ray diffraction analysis

Well-crystallized molybdenite flakes were embedded in epoxy resin and sliced into ~50-nm-thick foils using a Leica EM UC7 ultramicrotome equipped with a diamond knife. The cutting was performed perpendicular to the (001) plane of the molybdenite flakes and the obtained foils were put on carbon-coated Cu/Ni grids for TEM analysis. Micro-X-ray diffraction (micro-XRD) analysis was carried out on the exposed area of the sliced epoxy resin (Fig. 2a) using a Rigaku DMAX rapid diffraction system (Mo-Kα) at 50 kV and 90 mA. Micro-XRD patterns were collected using a 30-μm X-ray beam collimator. The stage oscillated about the ω-axis (2θ = 2–35°) and spun about the ϕ-axis to produce a maximum beam footprint of 90 μm on the sample.

Transmission electron microscopy analysis

The ~50-nm-thick molybdenite slices were further analyzed by TEM after plasma cleaning. HRTEM and scanning transmission electron microscopy (STEM) analyses were carried out at 200-kV voltage using an FEI Talos F200S field-emission transmission electron microscope coupled with two SuperX high-resolution energy-dispersive spectrometer (EDS) detectors and a high-angle annular dark-field

(HAADF) detector. The spatial resolution of the STEM mode was ~0.16 nm. Z-contrast images were acquired using a camera length of 160 mm to maximize the contrast variations between the different atoms in the HAADF images (Xu et al. 2014b, 2014c, 2015).

RESULTS

Phase identification and quantitative analysis

The molybdenite polytypes were identified by referring to theoretical mixtures of $2H_1$ and $3R$ polytypes calculated by Wickman and Smith (1970). In Fig. 2a, the sharp reflections at 16.31° (2.50 Å), 17.93° (2.27 Å), 22.36° (1.83 Å), and 24.98° (1.64 Å) in the micro-XRD pattern are attributed to the (102), (103), (105), and (106) planes of the $2H_1$-molybdenite (JCPDS card No. 73-1508 Mo-Kα), respectively. The broad peaks at 17.41° (2.34 Å), 18.61° (2.19 Å), 21.64° (1.89 Å), and 23.32° (1.76 Å) correspond to the (014), (015), (017), and (018) reflections of the $3R$-molybdenite (JCPDS card No. 75-0034 Mo-Kα), respectively. The unindexed reflections, e.g., 12.16° (3.35 Å) (Fig. 2a), are likely derived from the layered PbS precipitates that occur as a separate phase in the molybdenite. The relative intensities of the (103) and (105) reflections for the $2H_1$ polytype and the (014), (015), (017), and (018) reflections for the $3R$ polytype were chosen for quantitative analysis (Wickman and Smith 1970). The results suggest the co-existence of $2H_1$ and $3R$ polytypes in the investigated molybdenite with a calculated ratio of $2H_1/3R \approx 9{:}1$.

Chemical composition of the Pb-bearing molybdenite

Two occurrences of the Pb-bearing phase were identified in the backscattered electron (BSE) images (Figs. 1c, 1d). The galena inclusions are several micrometers

in length, >100 nm in thickness, and coexist with the molybdenite grains (Figs. 1c, S1d). The nano-scale Pb-bearing zones occur randomly within the molybdenite grains (Figs. 1d, S1f).

The EPMA results indicate a heterogeneous distribution of Pb in the molybdenite samples (Fig. 2b), reaching 0.59–1.33 wt.% in the Pb-bearing zones (Table 1). Owing to the large EPMA beam diameter (>1 μm), which is substantially larger than the nanoscale Pb-bearing zones, the Pb concentrations in these areas may be even higher (Figs.1d, S2). The Pb-poor molybdenite (Table 1) has close to stoichiometric Mo and S concentrations (60 wt.% Mo and 40 wt.% S). The EPMA mapping reveals that the Pb-bearing zones are commonly located in the cores of some molybdenite grains (Fig. 2b). The HAADF-STEM images reveal ~1-nm-wide bright bands in the Pb-bearing zones (open triangles in Fig. 2c). The elemental maps using the Pb L-line indicate that the Pb enrichment coincides with the bright bands in the host molybdenite (right side of Fig. 2c). The X-ray EDS spectra show that the bright bands are primarily composed of Mo, S, and Pb (Fig. 2d). The bright bands have a higher peak Pb intensity than the neighboring host molybdenite (Figs. S2i, S2j), which also indicates the higher Pb contents (Fig. 2d). Because the concentrations of other elements (e.g., O, C, and W) are negligible, the Pb-rich band is likely Pb-sulfide, Pb-bearing molybdenite, or metallic Pb (Figs. 2, S2).

Nano-scale features of layered PbS

Z-contrast images with atomic resolution were obtained to identify the mineral phases in the Pb-rich bands (Fig. 3a). The bright spots in the Z-contrast image (Fig. 3a) correspond to the positions of the atom columns along the beam direction. The plots of molybdenite (MoS_2) and PbS along the [010] zone axis are overlain on the

Z-contrast image. The intensity profile along the *c*-direction of the Z-contrast image shows that eight relatively weak Mo + S peaks are separated by two stronger Pb + S peaks (Fig. 3b). These features suggest that the sandwich-type MoS_2 sheets are separated by layered PbS sheets (Fig. 3a). The distances between the weak and strong peaks are ~0.62 nm and ~0.30 nm, corresponding to the fringe spacings along the *c*-axis of the molybdenite and layered PbS, respectively. The layered PbS has a similar fringe spacing to that of galena (i.e., ~0.30 nm), and can therefore be regarded as a distorted galena structure.

Crystallographic characteristics of the Pb-bearing molybdenite

The TEM image of the Pb-poor zone shows a smooth surface (Fig. 4a). The sharp and bright diffraction spots without specific extinction in the selected-area electron diffraction (SAED) pattern indicate well-crystallized $2H_1$-polytype molybdenite. In contrast, the surface of the Pb-bearing region (black open triangles in Figs. 4a and 4b) shows non-periodic features/contrast and its SAED pattern includes streaks (white arrows in Fig. 4a) between the *00l* and *h0l* diffraction spots. These streaks reflect highly disordered stacking sequences along the *c*-axis. The nano-beam electron diffraction (NBED) patterns further confirm that the Pb-poor area in the molybdenite belongs to an ordered $2H_1$ polytype and the Pb-rich area has disordered layer stacking. A 3*R* polytype is also identified in the vicinity of the Pb-rich area (Fig. 5). Nearly all of the investigated samples contain coexisting ordered (Figs. 4c, 4d) and disordered layer stacking domains (Figs. 4c, 4e), corresponding to the Pb-poor and Pb-bearing zones, respectively. The streaking diffraction observed in the SAED/FFT (Fast Fourier Transform) patterns of the Pb-bearing molybdenite reveals that the 3*R* polytype and disordered molybdenite usually occur in the same region (Figs. 4, 5),

corresponding to the broad reflections attributed to the 3*R* polytype in the micro-XRD pattern (Fig. 2a).

The HAADF-STEM image (Fig. 6a) shows 2, 4, and 6 layers of PbS pairs along the *c*-axis in the host molybdenite, corresponding to 1, 2, and 3 unit cells of layered PbS, respectively. In the STEM images, the [S-Mo-S] layers are completely (Fig. 6b, top) or partially (Fig. 6b, bottom) replaced by PbS. Pb-bearing domains also occur neighboring the Pb-poor domains and/or layered PbS in the host molybdenite (Fig. 6c), corresponding to the broad light band in the low-magnification STEM image (Fig. 7a). The enlarged area of Fig. 6b displays an intermediate state between the Pb-bearing molybdenite and 2-layer PbS (Fig. 6d). The mismatched structure results in the formation of crystal defects (e.g., dislocations) surrounding the layered PbS (open triangles in Fig. 6b). Pb was also observed to significantly diffuse under prolonged electron beam irradiation, further scavenging Pb from the host molybdenite into the layered precipitates (Fig. 7), as discussed in the following section.

DISCUSSION

Formation conditions for Pb-bearing phases in molybdenite

The sub-micro-scale galena commonly occurs as >100-nm inclusions in the interstices of molybdenite flakes and does not show an orientation relationship with the neighboring molybdenite (Figs. 1c, S1d). This galena probably formed by direct precipitation from a hydrothermal fluid in the interstitial spaces of the growing molybdenite, in accordance with previous studies (Ciobanu et al. 2013; Pasava et al. 2016). The HAADF-STEM images indicate that Pb ions can be incorporated into the molybdenite structure, as shown by the high-contrast regions in Fig. 6c. The incorporation of impurities in a growing mineral depends on the thermodynamic

conditions (e.g., temperature and pressure), crystallization rate, and similarity of the ionic properties (e.g., radius and charge) between the component ions and impurities (see Sunagawa 2005 and references therein). The prominently different ionic radii of Pb (Pb^{2+} = 1.29 Å, Pb^{4+} = 0.98 Å), S (S^{2-} = 1.84 Å), and Mo ions (Mo^{4+} = 0.65 Å) suggest that Pb incorporation causes lattice compression or expansion and disordered stacking in molybdenite (Fig. 4e). On the other hand, impurities are more likely to be incorporated under relatively high temperatures and rapid crystallization rates. High crystallization temperatures have been shown to provide an additional driving force for Pb incorporation into the molybdenite structure (c.f., Sunagawa 2005 and references therein).

The Pb-bearing molybdenite aggregates are commonly infilled with calcite (Fig. 1b) or closely coexist with calcite aggregates in the carbonatite dykes (Fig. S1c). The paragenesis suggests that the molybdenite formed simultaneously with or earlier than the calcite. Given that carbonatite dykes generally have high water contents (~15%), the melts that form from carbonatite dykes tend to have relatively low viscosities (Keppler 2003). In the Huanglongpu deposit, this low viscosity enabled the carbonatite melt to rapidly ascend to the near-surface (Xu et al. 2014a). The Pb-bearing molybdenite thus likely formed before or during melt ascent and rapidly cooled within the host carbonatite melt (Fig. 1), which is in accordance with the generally smaller grain size compared with porphyry-skarn hydrothermal systems in the East Qinling orogenic belt (Li and Pirajno 2017). In the present study, most of the Pb-bearing molybdenite occurs as cores within the molybdenite grains (Figs. 1d, 2b), suggesting that Pb was incorporated into the molybdenite at relatively high temperatures during initial crystallization. The high cooling rate also inhibited Pb migration out of molybdenite, resulting in a local enrichment of Pb up to several

weight percent. The relatively high crystallization temperature and rapid crystallization rate therefore provide a thermodynamic advantage for the formation of Pb-bearing molybdenite.

Genesis of layered PbS in molybdenite

Previous studies have suggested that layered PbS intergrown with coherent Bi-chalcogenides can form mixed-layer configurations (Cook et al. 2007a, 2007b; Ciobanu et al. 2009a). However, the layered PbS observed in the present study most likely formed by the exsolution of Pb from the Pb-bearing molybdenite. The STEM observations reveal that Pb diffusion occurs under electron beam irradiation with the gradual disappearance of the Pb-bearing region and formation of layered PbS in the molybdenite (Figs. 6c, 7). The observed 2–6 atomic-layer-thick PbS within the Pb-poor molybdenite (Figs. 6, S2) also suggests that the layered PbS likely formed by Pb diffusion during post-crystallization processes.

Minerals tend to exclude incompatible elements from their crystal lattice to minimize the Gibbs free energy in the mineral system during crystallization. As a result, incompatible elements generally occur in limited concentrations within the lattice of their host minerals (c.f., Sunagawa 2005 and references therein). In the present study, the dislocations (Fig. 6b) and disordered stacking (Fig. 4) induced by Pb incorporation significantly lowered the thermodynamical stability of the Pb-bearing molybdenite. As a result, the metastable Pb-bearing molybdenite solid solution (Fig. 6c) tended to decompose into layered PbS and Pb-poor molybdenite (Fig. 6d) by migration and local Pb enrichment (Fig. 7) after crystallization. Due to the anisotropy of the layered molybdenite structure, the linear thermal expansion coefficient of the *c*-direction is greater than that of the *a*- and *b*-directions

(El-Mahalawy and Evans 1976), which may affect the diffusion rates of Pb and result in the formation of layered-PbS precipitates along the (001) plane rather than the (*hk*0) planes. The exsolution of Pb along the (001) plane leads to a transformation of the metastable Pb-bearing S-Mo-S layers to layered PbS with a two-atomic-layer thickness (Fig. 6d).

The chemical composition and crystal structure results indicate that the 2–6 layers of Pb-S pairs are very similar to those of galena. Due to the spatial constraint of the S-Mo-S sandwich structure, the layered PbS structure is significantly distorted compared with the standard galena. The Pb-S distance (~3.0 Å) of the layered PbS is similar to the S-Mo-S height (~3.1 Å), which results in an epitaxial relationship between the exsolved layered PbS and molybdenite matrix. These mixed-layer compounds of PbS and MoS_2 exhibit a combination of a pseudo-tetragonal (*Q*) with a pseudo-hexagonal (*H*) layer (Jaszczak et al. 2016). The *Q* (PbS-type) layer is a (100) slab of the PbS/NaCl archetype, 2n (n ≥ 1) atoms thick, similar to previously reported complex cylindrite group crystals $[(MX)_{1+y}]m(TX_2)_n$ (with M = Sn, Pb, Sb, and Bi, T = Ti, V, Nb, and Mo, and X = S and Se) (Williams and Hyde 1988; Lin et al. 2008; Makovicky et al. 2008; Garbrecht et al. 2011; Jaszczak et al. 2016).

Based on the above discussions, the layered PbS in molybdenite was proposed to forms in the following scenario (Fig. 8). Up to several weight percent of Pb was incorporated into the structure of molybdenite during the initial stage of crystallization (Fig. 8a). The incorporation of Pb atoms caused lattice expansion and screw dislocations (Fig. 6b), and further led to 3*R*/disordered stacking (Figs. 4, 5). Pb migration and enrichment at the grain boundaries or defects led to the formation of local Pb-bearing and Pb-poor molybdenite domains (Fig. 8b). The exsolution of Pb from the sandwiched Pb-bearing molybdenite led to the formation of layered PbS

along the (001) plane of molybdenite (Fig. 8c). Due to space restrictions of the molybdenite unit cell, the newly formed PbS shows a periodic layered structure with two atomic layers along the *c*-direction (Fig. 8c). The host molybdenite also transformed from a Pb-bearing 3*R*/disordered structure to a Pb-poor ordered $2H_1$ polytype. The incorporation of Pb and formation of nano-scale layered PbS by post-crystallization exsolution within molybdenite therefore led to the heterogeneous distribution of Pb in the molybdenite (Figs. 1d, 2b).

IMPLICATIONS

Trace elements in molybdenite can provide important constraints on the evolution processes and dating of a wide range of geological events. The behavior of incompatible trace elements tends to be more complicated than that of compatible trace elements in molybdenite. A better understanding of the behavior of incompatible trace elements is therefore of high importance for interpreting the related geochemical data. Recent nanoSIMS evidence has demonstrated significant Pb trapping by molybdenite (Rollog et al. 2019, 2020). The present study also shows a heterogeneous distribution of typically incompatible Pb in natural molybdenite. These findings provide important insight into the behavior of other incompatible elements within host minerals to better interpret the related geological data. For example, the reliability of ^{187}Re-^{187}Os isotopic data for molybdenite is based on the assumption that Re and Os are immobile and heterogeneously distributed within molybdenite (Stein et al. 2001, 2003). Previous studies suggested that incompatible radiogenic ^{187}Os is likely to be more mobile and stored in the micro-defects of molybdenite compared with parent ^{187}Re and may therefore become decoupled over time on the micrometer scale (Stein et al. 2001, 2003). This provides an explanation of why in-situ ICP-MS spot dating of

molybdenite consistently fails (Stein et al. 2003). The behavior of Pb in natural molybdenite can thus serve as a proxy for understanding the heterogeneous distribution and mobility of Os and other relatively incompatible trace elements in molybdenite.

Franckeite is a naturally occurring SnS_2/PbS van der Waals heterostructure and is a promising material for emerging energy storage technology and near-infrared photodetectors (Molina-Mendoza et al. 2017; Vělický et al. 2017). Synthetic MoS_2/PbS van der Waals heterostructures have been used as infrared memory devices (Wang et al. 2018). Natural Pb-bearing molybdenite (MoS_2)/layered-PbS van der Waals heterostructures may therefore also have relevant properties that can serve as a natural model for the synthesis of layered MoS_2/PbS heterostructures.

ACKNOWLEDGMENTS

This study was financially supported by National Natural Science Foundation of China (Grant Nos. 41772039, 41921003 and 41825003), CAS Key Research Program of Frontier Sciences (Grant No. QYZDJ-SSW-DQC023), Department of Science and Technology of Guangdong Province: 2017GC010578 and Science and Technology Planning Project of Guangdong Province, China: 2020B1212060055. The authors thank Dr. David Dolejs for handling this paper, and Dr. Olga Plotinskaya and an anonymous reviewer for reviewing the manuscript and providing constructive comments and suggestions.

REFERENCES

Barra, F., Deditius, A., Reich, M., Kilburn, M.R., Guagliardo, P., and Roberts, M.P. (2017) Dissecting the Re-Os molybdenite geochronometer. Scientific Reports, 7, 16054.

Ciobanu, C.L., Pring, A., Cook, N.J., Self, P., Jefferson, D., Dima, G.I., and Melnikov, V. (2009) Chemical-structural modularity in the tetradymite group: A HRTEM study. American Mineralogist, 94, 517–534.

Ciobanu, C.L., Cook, N.J., Kelson, C.R., Guerin, R., Kalleske, N., and Danyushevsky, L. (2013) Trace element heterogeneity in molybdenite fingerprints stages of mineralization. Chemical Geology, 347, 175–189.

Cook, N.J., Ciobanu, C.L., Stanley, C.J., Paar, W.H., and Sundblad, K. (2007a) Compositional data for Pb-Bi tellurosulphides. The Canadian Mineralogist, 45, 417–435.

Cook, N.J., Ciobanu, C.L., Wagner, T., and Stanley, C.J. (2007b) Minerals of the system Bi-Te-Se-S related to the tetradymite archetype: Review of classification and compositional variation. The Canadian Mineralogist, 45, 665–708.

Du, A., Wu, S., Sun, D., Wang, S., Qu, W., Markey, R., Stain, H., Morgan, J., and Malinovskiy, D. (2004) Preparation and Certification of Re-Os Dating Reference

382 Materials: Molybdenites HLP and JDC. Geostandards and Geoanalytical
383 Research, 28, 41–52.

384 El-Mahalawy, S., and Evans, B. (1976) The thermal expansion of 2*H*-MoS_2,
385 2*H*-$MoSe_2$ and 2*H*-WSe_2 between 20 and 800 ℃. Journal of Applied
386 Crystallography, 9, 403-406.

387 Fleischer, M. (1959) The geochemistry of rhenium, with special reference to its
388 occurrence in molybdenite. Economic Geology, 54, 1406–1413.

389 Frondel, J.W., and Wickman, F.E. (1970) Molybdenite polytypes in theory and
390 occurrence .Ⅱ. Some naturally-occurring polytypes of molybdenite. American
391 Mineralogist, 55, 1857-1875.

392 Grabezhev, A.I., and Voudouris, P.C. (2014) Rhenium distribution in molybdenite
393 from the Vosnesensk porphyry Cu ± (Mo,Au) deposit (Southern Urals, Russia).
394 The Canadian Mineralogist, 52, 671–686.

395 Garbrecht, M., Spiecker, E., Tillmann, K., and Jager, W. (2011) Quantitative atom
396 column position analysis at the incommensurate interfaces of a $(PbS)_{1.14}NbS_2$
397 misfit layered compound with aberration-corrected HRTEM. Ultramicroscopy,
398 111, 245-250.

399 Huang D.H, Wang Y.C, Nie F.J, and Jiang X.J. (1985) A new type of molybdenum
400 deposit: Geologic characteristics and metallogenic mechanism of Huanglongpu

carbonatite vein-type of molybdenum (lead) deposit, Shaanxi. Acta Geologica Sinica, 59, 241-257. (in Chinese with English abstract)

Jaszczak, J.A., Rumsey, M.S., Bindi, L., Hackney, S.A., Wise, M.A., Stanley, C.J., and Spratt, J.(2016) Merelaniite, $Mo_4Pb_4VSbS_{15}$, a new molybdenum-essential member of the cylindrite group, from the merelani tanzanite deposit, lelatema mountains, Manyara region, Tanzania. Minerals, 6, 115.

Keppler, H. (2003) Water solubility in carbonatite melts. American Mineralogist, 88, 1822-1824.

Li, N. Pirajno, F. (2017) Early Mesozoic Mo mineralization in the Qinling Orogen: An overview. Ore Geology Reviews, 81, 431-450.

Lin, Q., Heideman, C.L., Nguyen, N., Zschack, P., Chiritescu, C., Cahill, D.G., and Johnson, D.C. (2008) Designed synthesis of families of misfit-layered compounds. European Journal of Inorganic Chemistry, 15, 2382-2385.

Lin, Y.C., Dumcencon, D.O., Huang, Y.S., and Suenaga, K. (2014a) Atomic mechanism of the semiconducting-to-metallic phase transition in single-layered MoS_2. Nature Nanotechnology, 9, 391-396.

Lin, Y.C., Dumcenco, D.O., Komsa, H.P., Niimi, Y., Krasheninnikov, A.V., Huang, Y.S., and Suenaga, K. (2014b) Properties of individual dopant atoms in

single-layer MoS_2: atomic structure, migration, and enhanced reactivity. Advanced Materials, 26, 2857-2861.

Makovicky, E., Petricek, V., Dusek, M., and Topa, D. (2008) Crystal structure of a synthetic tin-selenium representative of the cylindrite structure type. American Mineralogist, 93, 1787-1798.

Mccandless, T.E., Ruiz, J., and Campbell, A.R. (1993) Rhenium behavior in molybdenite in hypogene and near-surface environments: Implications for Re-Os geochronometry. Geochimica et Cosmochimica Acta, 57, 889-905.

Molina-Mendoza, A.J., Giovanelli, E., Paz, W.S., Nino, M.A., Island, J.O., Evangeli, C., Aballe, L., Foerster, M., van der Zant, H.S.J., Rubio-Bollinger, G., Agrait, N., Palacios, J.J., Perez, E.M., and Castellanos-Gomez, A. (2017) Franckeite as a naturally occurring van der Waals heterostructure. Nature Communications, 8, 14409.

McCandless, T.E., Ruiz, J., and Campbell, A.R. (1993) Rhenium behavior in molybdenite in hypogene and near-surface environments: Implications for Re-Os geochronometry. Geochimica et Cosmochimica Acta, 57, 889–905.

Newberry, R.J.J. (1979a) Polytypism in molybdenite (I): a non-equilibrium impurity-induced phenomenon. American Mineralogist, 64, 758–769.

437 Newberry, R.J.J. (1979b) Polytypism molybdenite (II): relationships between
438 polytypism, ore deposition/alteration stages and rhenium coitents. American
439 Mineralogist, 64, 768–775.

440 Pašava, J., Svojtka, M., Veselovský, F., Ďurišová, J., Ackerman, L., Pour, O., Drábek,
441 M., Halodová, P., and Haluzová, E. (2016) Laser ablation ICPMS study of trace
442 element chemistry in molybdenite coupled with scanning electron microscopy
443 (SEM) — An important tool for identification of different types of
444 mineralization. Ore Geology Reviews, 72, 874–895.

445 Pennycook, S.J. (2002) Structure determination through Z-contrast microscopy.
446 Advances in Imaging Electron Physics, 123, 173-206.

447 Petruk, W. (1965) Mineralogy of the Mount Pleasant tin deposit, New Brunswick. In
448 Canada Mines Branch Tech, pp. 1–35.

449 Plotinskaya, O.Y., Abramova, V.D., Groznova, E.O., Tessalina, S.G., Seltmann, R.,
450 and Spratt, J. (2018) Trace-element geochemistry of molybdenite from porphyry
451 Cu deposits of the Birgilda-Tomino ore cluster (South Urals, Russia).
452 Mineralogical Magazine, 82, S281-S306.

453 Plotinskaya, O. Y., Shilovskikh, V. V., Najorka, J., Kovalchuk, E. V., Seltmann, R.,
454 and Spratt, J. (2019) Grain-scale distribution of molybdenite polytypes versus
455 rhenium contents: μXRD and EBSD data. Mineralogical Magazine, 83, 639-644.

456 Rollog, M., Cook, N.J., Guagliardo, P., Ehrig, K., Ciobanu, C.L., and Kilburn, M.
457 (2019) Detection of Trace Elements/Isotopes in Olympic Dam Copper
458 Concentrates by nanoSIMS. Minerals, 9, 336.

459 Rollog, M., Cook, N.J., Guagliardo, P., Ehrig, K., and Kilburn, M. (2020)
460 Radionuclide distributions in Olympic Dam copper concentrates: The
461 significance of minor hosts, incorporation mechanisms, and the role of mineral
462 surfaces. Minerals Engineering, 148, 106176.

463 Song, W., Xu, C., Qi, L., Zhou, L., Wang, L., and Kynicky, J. (2015) Genesis of
464 Si-rich carbonatites in Huanglongpu Mo deposit, Lesser Qinling orogen, China
465 and significance for Mo mineralization. Ore Geology Reviews, 64, 756-765.

466 Song, W., Xu, C., Smith, M.P., Kynicky, J., Huang, K., Wei, C., Zhou, L., and Shu, Q.
467 (2016) Origin of unusual HREE-Mo-rich carbonatites in the Qinling orogen,
468 China. Scientific Reports, 6, 37377

469 Stein, H., Scherstén, A., Hannah, J., and Markey, R. (2003) Subgrain-scale
470 decoupling of Re and 187Os and assessment of laser ablation ICP-MS spot
471 dating in molybdenite. Geochimica et Cosmochimica Acta, 67, 3673–3686.

472 Stein, H.J., Markey, R.J., Morgan, J.W., Du, A., and Sun, Y. (1997) Highly precise
473 and accurate Re-Os ages for molybdenite from the East Qinling molybdenum
474 belt, Shaanxi Province, China. Economic Geology, 92, 827–835.

475 Stein, H.J., Markey, R.J., Morgan, J.W., Hannah, J.L., and Schersten, A. (2001) The
476 remarkable Re-Os chronometer in molybdenite: how and why it works. Terra
477 Nova, 13, 479–486.

478 Sunagaw, I. (2005) Crystals: growth, morphology, and perfection, 308 p. Cambridge
479 University Press, UK.

480 Terada, K., Osaki, S., Ishihara, S., and Kiba, T. (1971) Distribution of rhenium in
481 molybdenites from Japan. Geochemical Journal, 4, 123–141.

482 Vělický, M., Toth, P.S., Rakowski, A.M., Rooney, A.P., Kozikov, A., Woods, C.R.,
483 Mishchenko, A., Fumagalli, L., Yin, J., Zolyomi, V., Georgiou, T., Haigh, S.J.,
484 Novoselov, K.S., and Dryfe, R.A.W. (2017) Exfoliation of natural van der Waals
485 heterostructures to a single unit cell thickness. Nature Communications, 8,
486 14410.

487 Voudouris, P.C., Melfos, V., Spry, P.G., Bindi, L., Kartal, T., Arikas, K., Moritz, R.,
488 and Ortelli, M. (2009b) Rhenium-rich molybdenite and rheniite in the Pagoni
489 Rachi Mo-Cu-Te-Ag-Au prospect, Northern Greece: Implications for the Re
490 geochemistry of porphyry-style Cu-Mo and Mo mineralization. The Canadian
491 Mineralogist, 47, 1013-1036.

492 Wang, Q.S., Wen, Y., Cai, K.M., Cheng, R.Q., Yin, L., Zhang, Y., Li, J., Wang, Z.X.,
493 Wang, F., Wang, F.M., Shifa, T.A., Jiang, C., Yang, H., and He, J. (2018)

494 Nonvolatile infrared memory in MoS_2/PbS van der Waals heterostructures.
495 Science Advances, 4, eaap7916.

496 Williams, T.B., and Hyde, B.G. (1988) Electron-Microscopy of Cylindrite and
497 Franckeite. Physics and Chemistry of Minerals, 15, 521-544.

498 Xu, C., Chakhmouradian, A.R., Taylor, R.N., Kynicky, J., Li, W.B., Song, W.L., and
499 Fletcher, I.R. (2014a) Origin of carbonatites in the South Qinling orogen:
500 Implications for crustal recycling and timing of collision between the South and
501 North China Blocks. Geochimica et Cosmochimica Acta, 143, 189-206.

502 Xu, C., Song, W., Qi, L., and Wang, L. (2009) Geochemical characteristics and
503 tectonic setting of ore-bearing carbonatites in Hunglongpu Mo ore field. Acta
504 Petrologica Sinica, 25, 422-430. (in Chinese with English abstract)

505 Xu, H., Shen, Z., Konishi, H., and Luo, G. (2014b) Crystal structure of
506 Guinier-Preston zones in orthopyroxene: Z-contrast imaging and ab inito study.
507 American Mineralogist, 99, 2043–2048.

508 Xu, H., Shen, Z., and Konishi, H. (2014c) Si-magnetite nano-precipitates in silician
509 magnetite from banded iron formation: Z-contrast imaging and ab initio study.
510 American Mineralogist, 99, 2196–2202.

511 Xu, H., Shen, Z., and Konishi, H. (2015) Natural occurrence of monoclinic Fe_3S_4
512 nano-precipitates in pyrrhotite from the Sudbury ore deposit: a Z-contrast

imaging and density functional theory study. Mineralogical Magazine, 79, 377–385.

Figure Captions:

FIGURE 1. Photomicrographs (**a-b**) and backscattered electron (BSE) images (**c-d**) showing the occurrences of molybdenite features in the carbonatite veins. (**a**) Molybdenite aggregates of thin flakes in carbonatite veins. (**b**) Reflected light images of dendritic molybdenite clusters (50–80 μm in diameter) that closely coexist with calcite. (**c**) Micrometer galena inclusion within molybdenite grain. (**d**) Nanoscale Pb-bearing zones within molybdenite grain. Cal, calcite; Gn, galena; Mol, molybdenite.

FIGURE 2. X-ray diffraction pattern and nano-scale features of Pb-bearing molybdenite. (**a**) Micro-X-ray diffraction pattern of the $2H_1$ and $3R$ polytype molybdenite. The X-ray diffraction pattern area (epoxy resin with embedded molybdenite) was obtained from an ultrathin section for transmission electron microscopy (schematic shown in upper right). (**b**) Heterogeneous Pb distribution within molybdenite of the inserted area (top left), revealed by X-ray intensity mapping. (**c**) High-angle annular dark-field scanning transmission electron microscopy image shows ~1-nm-wide bright bands in the Pb-bearing zones of molybdenite, as indicated by the open triangles (left) and the corresponding elemental maps of the Pb-L line of the target Pb-bearing zones (right). (**d**) X-ray energy-dispersive spectrum collected from the Pb-enriched area in (**c**). The Cu signal is from the Cu grid.

538 **FIGURE 3.** Atom-scale features of the Pb-bearing zones in molybdenite. (**a**)
539 Layered-PbS in the Pb-bearing zones in a high-angle annular dark-field scanning
540 transmission electron microscopy (HAADF-STEM) image. The ball-and-stick model
541 displays the corresponding structures of molybdenite (MoS_2) and layered PbS along
542 the [010] zone axis. The blue, green, and yellow spheres represent Pb, Mo, and S
543 atoms, respectively. (**b**) Atom intensity distribution of the layered-PbS band and
544 neighboring molybdenite sheets along the *c*-direction, as indicated by the red line. The
545 intensity (I) of the atom spots is proportional to the atomic number (Z) and the
546 number of atoms (m) along the beam direction (i.e., $I \sim mZ^n$) in the HAADF-STEM
547 images (Pennycook 2002).
548
549 **FIGURE 4.** Z-contrast images with corresponding transmission electron microscope
550 (TEM) images and selected-area electron diffraction (SAED) patterns collected from
551 a Pb-poor zone (white dotted circle) and Pb-bearing zone (white solid circle) along
552 the [010] zone axis within a single molybdenite crystal. (**a**) Low-magnification
553 high-angle annular dark-field scanning transmission electron microscopy
554 (HAADF-STEM), TEM images, and the corresponding SAED patterns of Pb-poor
555 and Pb-bearing molybdenite. (**b**) HAADF-STEM image of another Pb-bearing
556 molybdenite particle. (**c**) Enlarged HRTEM image from the white dotted square in b.
557 (**d**) FFT patterns from the Pb-poor (white dotted square in **c**) and (**e**) Pb-bearing zones
558 (white solid square in **c**). The black open triangles in (**a**) and (**b**) indicate the Pb-rich
559 band.
560
561 **FIGURE 5.** (**a**) High-angle annular dark-field scanning transmission electron
562 microscopy (HAADF-STEM) image of Pb-bearing molybdenite and nano-beam

563 electron diffraction (NBED) patterns (1–8) of different areas of the molybdenite. (**b-c**)
564 Corresponding STEM–energy-dispersive spectroscopy element maps of S and Pb.
565 The NBED patterns of the selected area (~10 nm per spot) in (**a**) show
566 2*H*-molybdenite in the Pb-poor domain (1, 2), disordered stacking in the Pb-rich
567 domain (3–5, 8), and the 3*R*-molybdenite near the Pb-rich band (6, 7).
568
569 **FIGURE 6.** Nano-scale and atomic-scale features of the layered PbS precipitates
570 distributed along the *c*-axis of the host molybdenite. (**a**) 2, 4, and 6 layers of PbS
571 distributed in Pb-bearing molybdenite. (**b**) High density of defects around the layered
572 PbS, as indicated by the triangle arrows. (**c**) High-resolution high-angle annular
573 dark-field scanning transmission electron microscopy (HAADF-STEM) image
574 showing layered PbS stacked along the *c*-axis in the Pb-bearing molybdenite. (**d**)
575 Atomic resolution HAADF-STEM image displaying the transformation of the
576 S-Mo-S sandwich structure to an NaCl-type layered PbS. The ball-and-stick model
577 displays the corresponding structures of molybdenite (MoS_2) and layered PbS along
578 the [010] zone-axis.
579
580 **FIGURE 7.** High-angle annular dark-field scanning transmission electron microscopy
581 (HAADF-STEM) images and corresponding energy-dispersive spectroscopy (EDS)
582 mapping and profile of the Pb-bearing molybdenite. (**a-b**) STEM images show a
583 relatively broad light band (**a**) and narrow light band (**b**) after 20 min of electron
584 beam irradiation within the host molybdenite. (**c**) STEM-EDS element maps of Mo
585 and Pb in (**a**). (**d**) EDS profile of the Pb-L spectrum shows the diffusion of Pb atoms
586 during EDS mapping. EDS profiles 1 and 2 were collected from the top down in
587 images (**a**) and (**b**), respectively.

588

589 **FIGURE 8.** Schematic diagram showing the transformation of Pb-bearing
590 molybdenite to layered PbS and Pb-poor molybdenite. The red, green, and yellow
591 spheres represent Pb, Mo, and S atoms, respectively. The blue dotted circles in the
592 [S-Mo-S] structure indicate S vacancies.

593

Table 1. Representative composition of major elements of molybdenite from the Huanglongpu Mo-Pb ore deposit based on electron microprobe analysis.

wt.%	Pb-poor zone						Pb-bearing zone			
	1	2	3	4	5	Avg.	1	2	3	Avg.
Mo	59.94	59.92	59.86	60.80	59.62	60.03	58.38	59.01	58.56	58.65
S	40.05	40.03	39.44	40.49	39.55	39.91	38.52	39.12	39.21	38.95
Fe	0.02	0.02	0.15	0.08	0.10	0.07	0.11	0.03	0.05	0.06
Ca	bdl	bdl	bdl	bdl	bdl	bdl	0.03	0.10	0.03	0.05
Re	0.04	0.03	0.05	0.03	0.03	0.04	0.05	0.09	0.06	0.07
Pb	bdl	bdl	bdl	bdl	bdl	bdl	1.33	0.75	0.59	0.89
Total	100.05	100.00	99.50	101.40	99.30	100.05	98.42	99.10	98.50	98.67
Calculated formulas										
Mo	0.9991	0.9991	0.9953	0.9974	0.9969	0.9977	0.9848	0.9885	0.9922	0.9887
S	2.0028	2.0025	1.9673	1.9929	1.9838	1.9898	1.9494	1.9661	1.9930	1.9699
Fe	0.0006	0.0006	0.0043	0.0023	0.0029	0.0020	0.0032	0.0009	0.0015	0.0017
Ca	-	-	-	-	-	-	0.0012	0.0040	0.0012	0.0020
Re	0.0003	0.0003	0.0004	0.0003	0.0003	0.0003	0.0004	0.0008	0.0005	0.0006
Pb	-	-	-	-	-	-	0.0104	0.0058	0.0046	0.0070

Note: Chemical formulas are calculated based on a normalized 100% for the total cations (i.e., Mo, Fe, Re, Ca, and Pb). As, Zr, Cu, and W are below the detection limit (bdl) in all of the spot analyses.

FIGURE 1

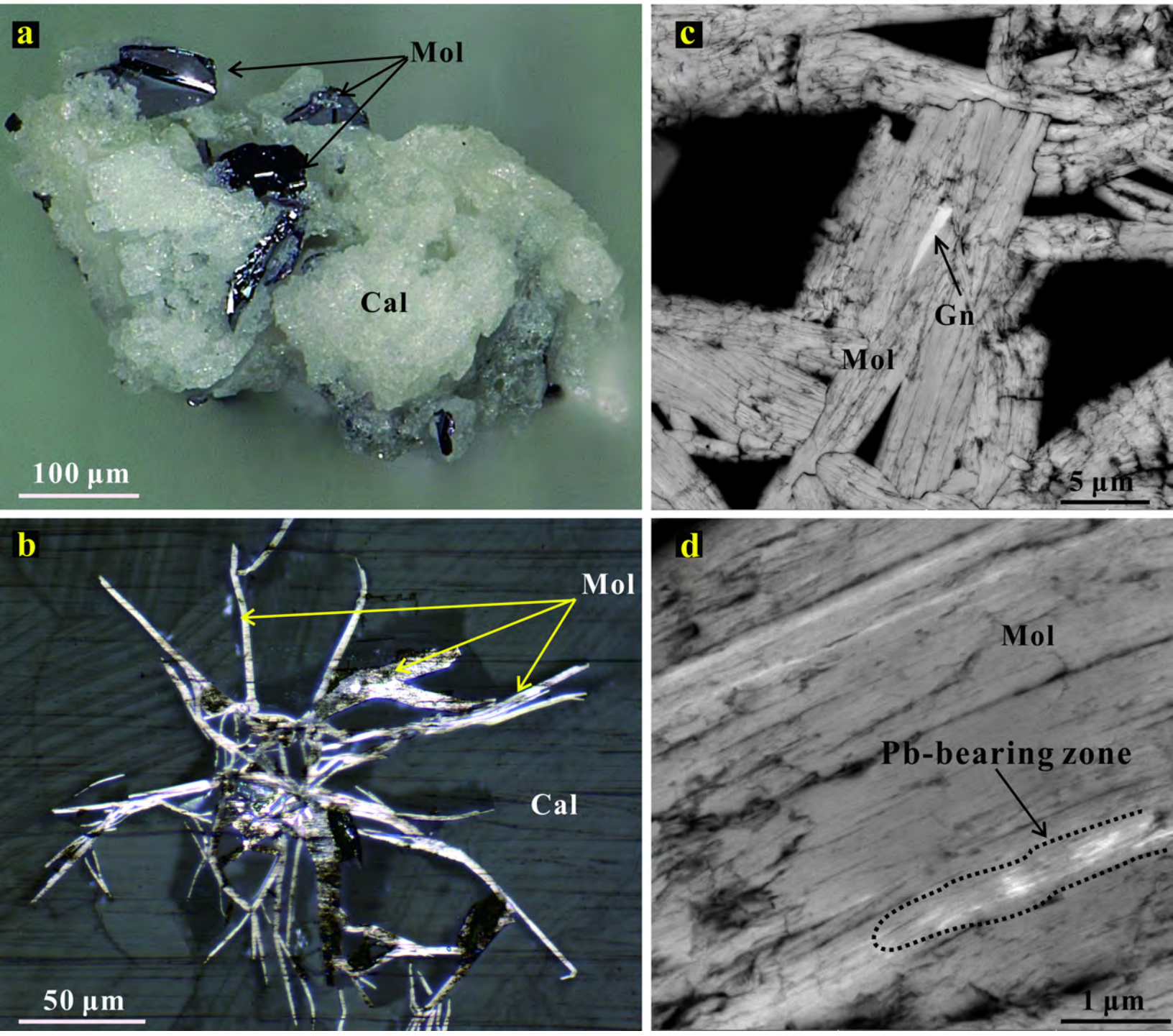
a
Mol
Cal
100 µm
c
Gn
Mol
5 µm
b
Mol
Cal
50 µm
d
Mol
Pb-bearing zone
1 µm

FIGURE 2

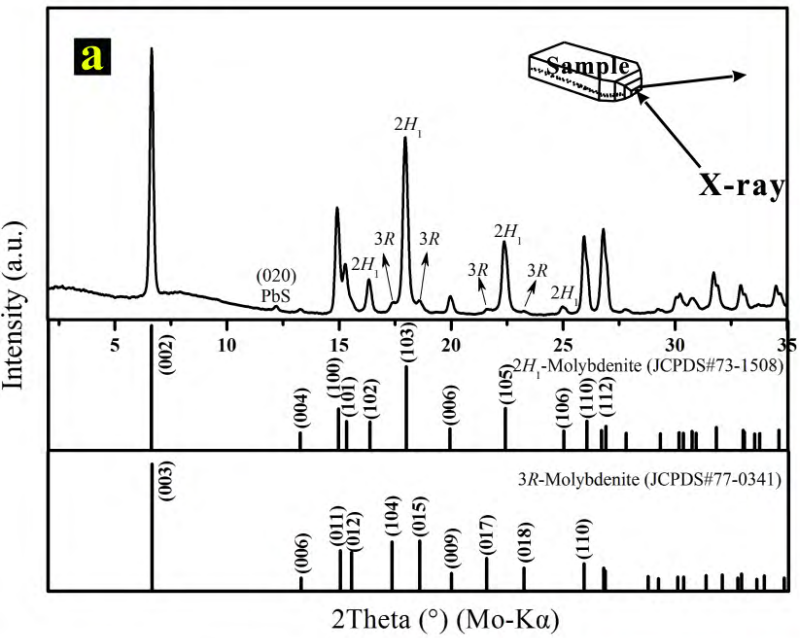
a
Sample
X-ray
$2H_1$
3R
(020)
PbS
Intensity (a.u.)
5
10
15
20
25
30
35
(002)
(103)
$2H_1$-Molybdenite (JCPDS#73-1508)
(004)
(100)
(101)
(102)
(006)
(105)
(106)
(110)
(112)
3R-Molybdenite (JCPDS#77-0341)
(003)
(006)
(011)
(012)
(104)
(015)
(009)
(017)
(018)
(110)
2Theta (°) (Mo-Kα)

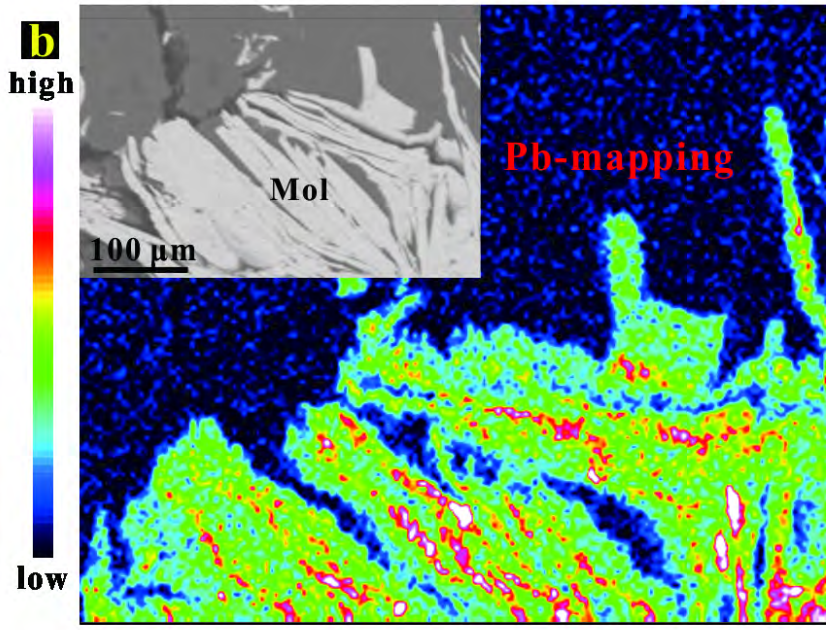
b
high
low
Mol
100 μm
Pb-mapping

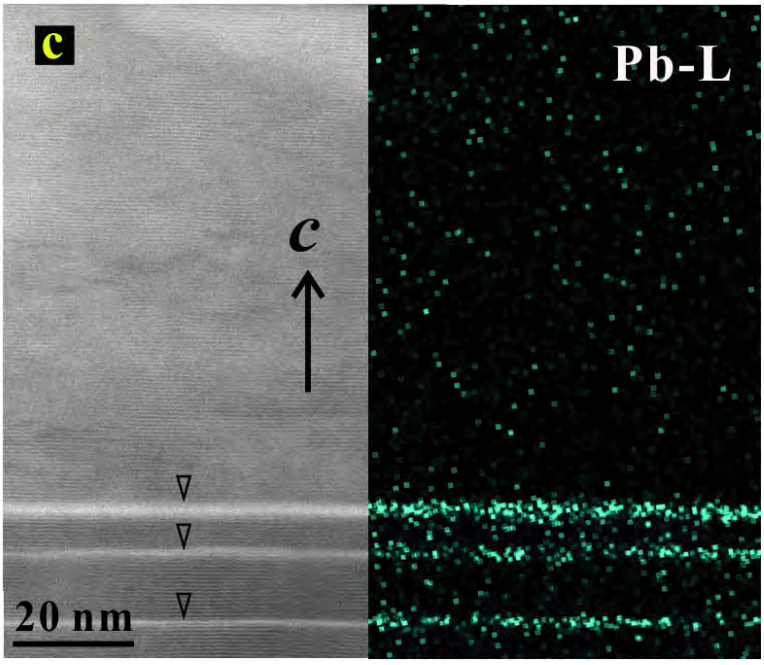
c
Pb-L
c
20 nm

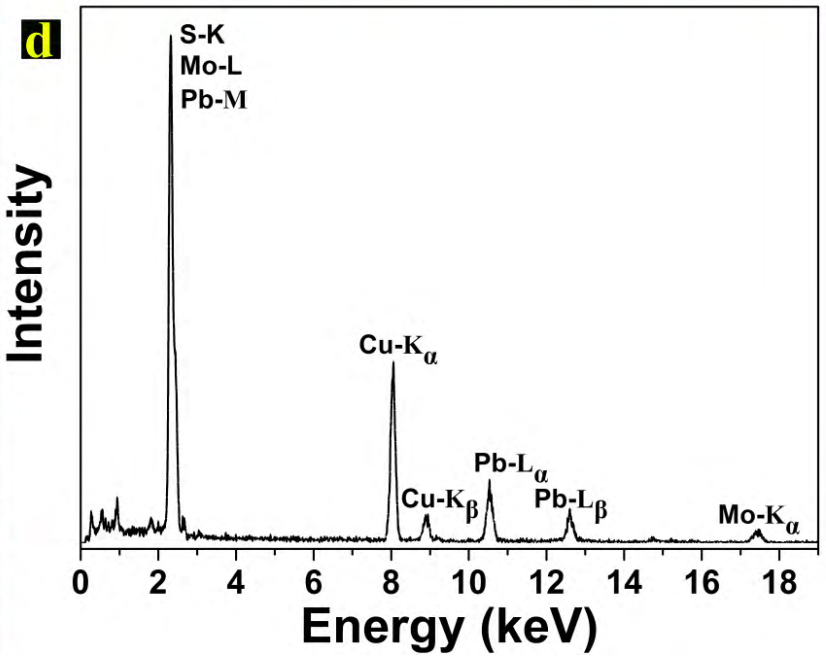
d
S-K
Mo-L
Pb-M
Cu-Kα
Cu-Kβ
Pb-Lα
Pb-Lβ
Mo-Kα
Intensity
0
2
4
6
8
10
12
14
16
18
Energy (keV)

FIGURE 3

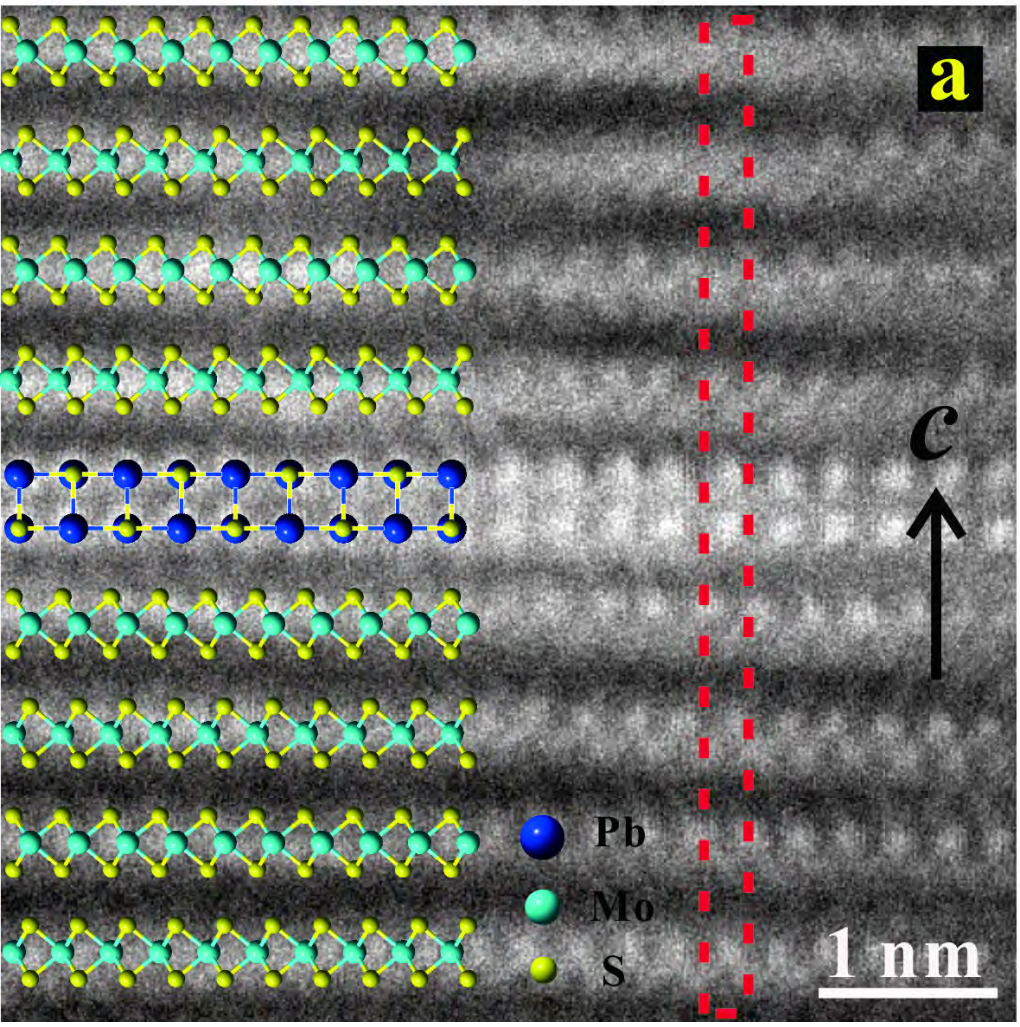
a
c
Pb
Mo
S
1 nm

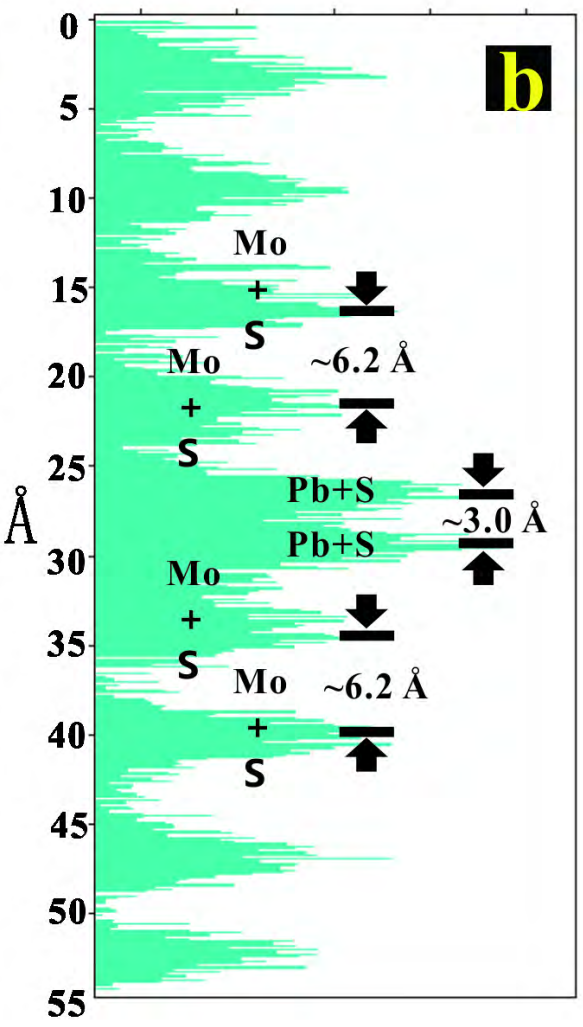
b
Å
0
5
10
15
20
25
30
35
40
45
50
55
Mo + S
~6.2 Å
Mo + S
Pb+S
~3.0 Å
Pb+S
Mo + S
Mo + S
~6.2 Å

FIGURE 4

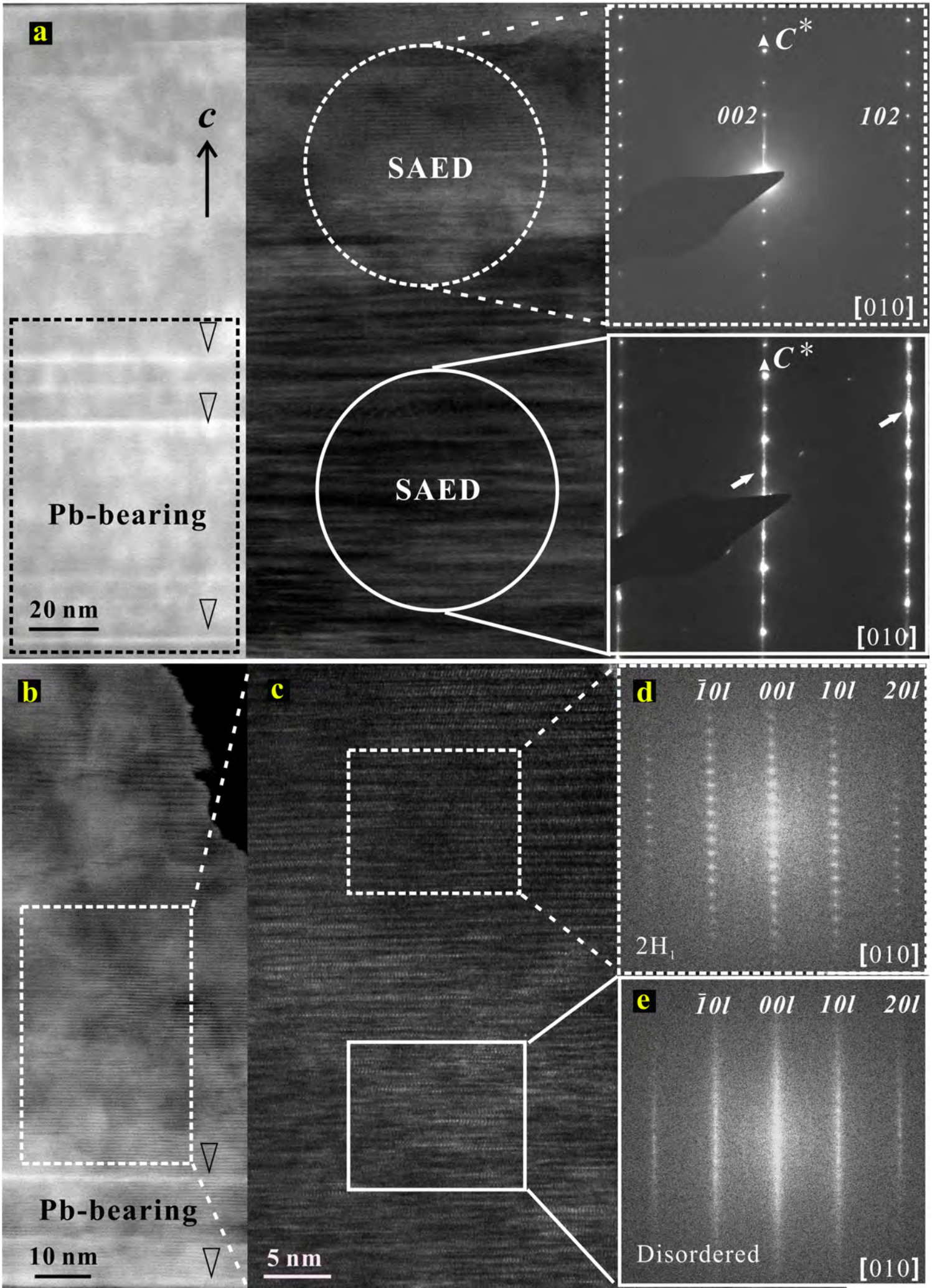
a
c
SAED
C*
002
102
[010]
Pb-bearing
20 nm
SAED
C*
[010]
b
c
d
$\bar{1}01$ 001 101 201
$2H_1$
[010]
Pb-bearing
10 nm
5 nm
e
$\bar{1}01$ 001 101 201
Disordered
[010]

FIGURE 5

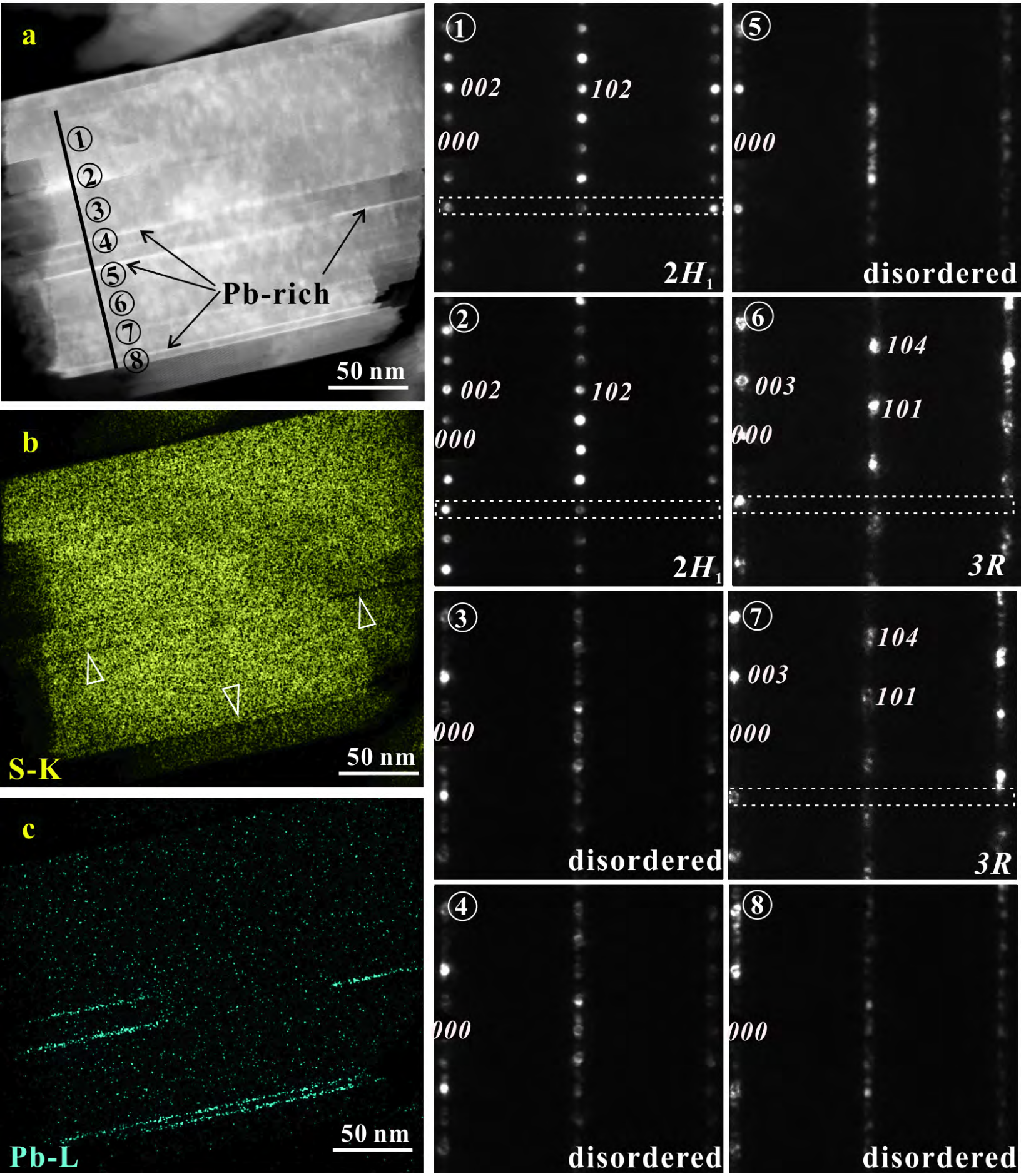
a
①
②
③
④
⑤
⑥
⑦
⑧
Pb-rich
50 nm
b
S-K
50 nm
c
Pb-L
50 nm
① 002 102 000 2H1
⑤ 000 disordered
② 002 102 000 2H1
⑥ 104 003 101 000 3R
③ 000 disordered
⑦ 104 003 101 000 3R
④ 000 disordered
⑧ 000 disordered

FIGURE 6

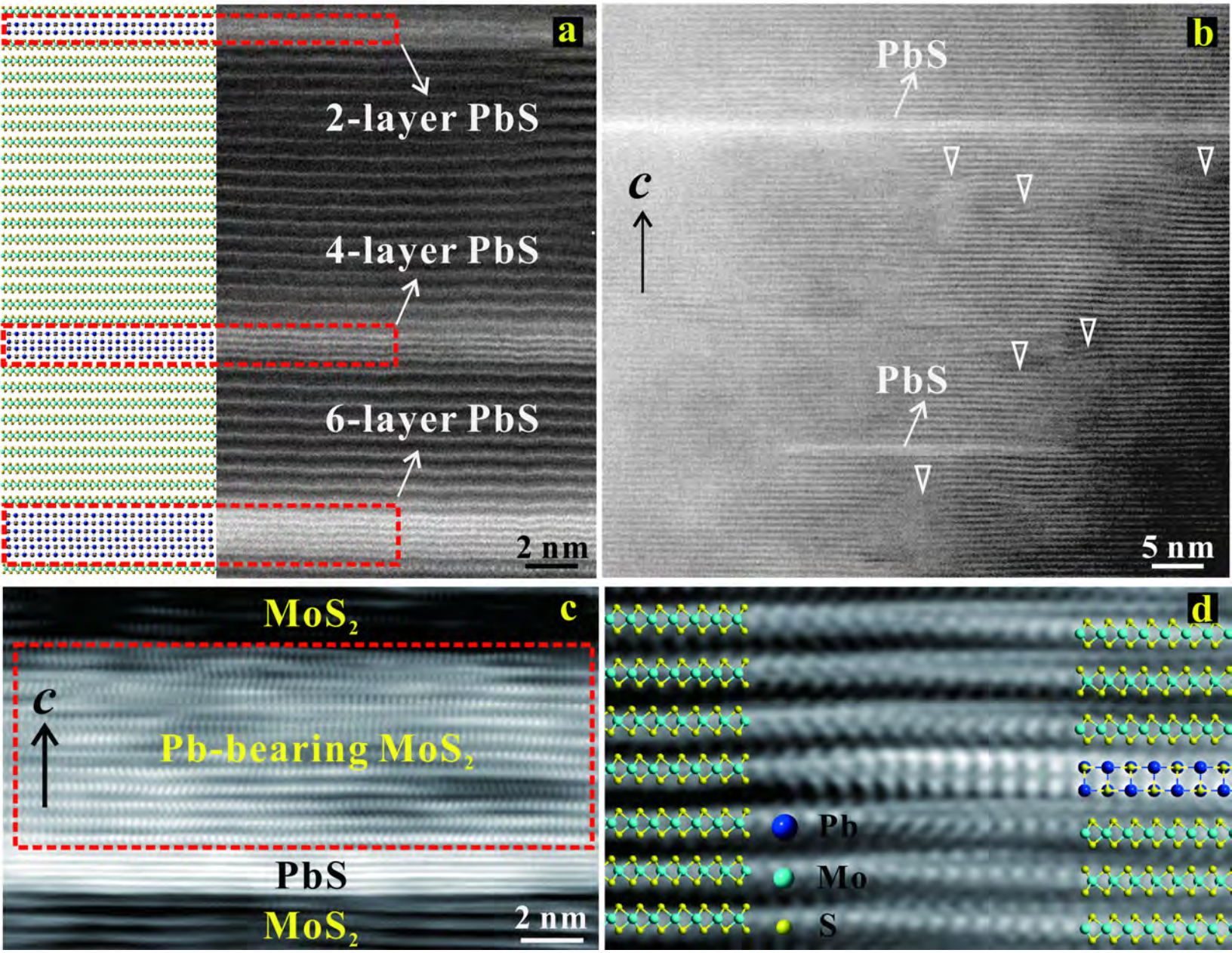
a
2-layer PbS
4-layer PbS
6-layer PbS
2 nm
b
PbS
c
PbS
5 nm
c
MoS2
c
Pb-bearing MoS2
PbS
MoS2
2 nm
d
Pb
Mo
S

FIGURE 7

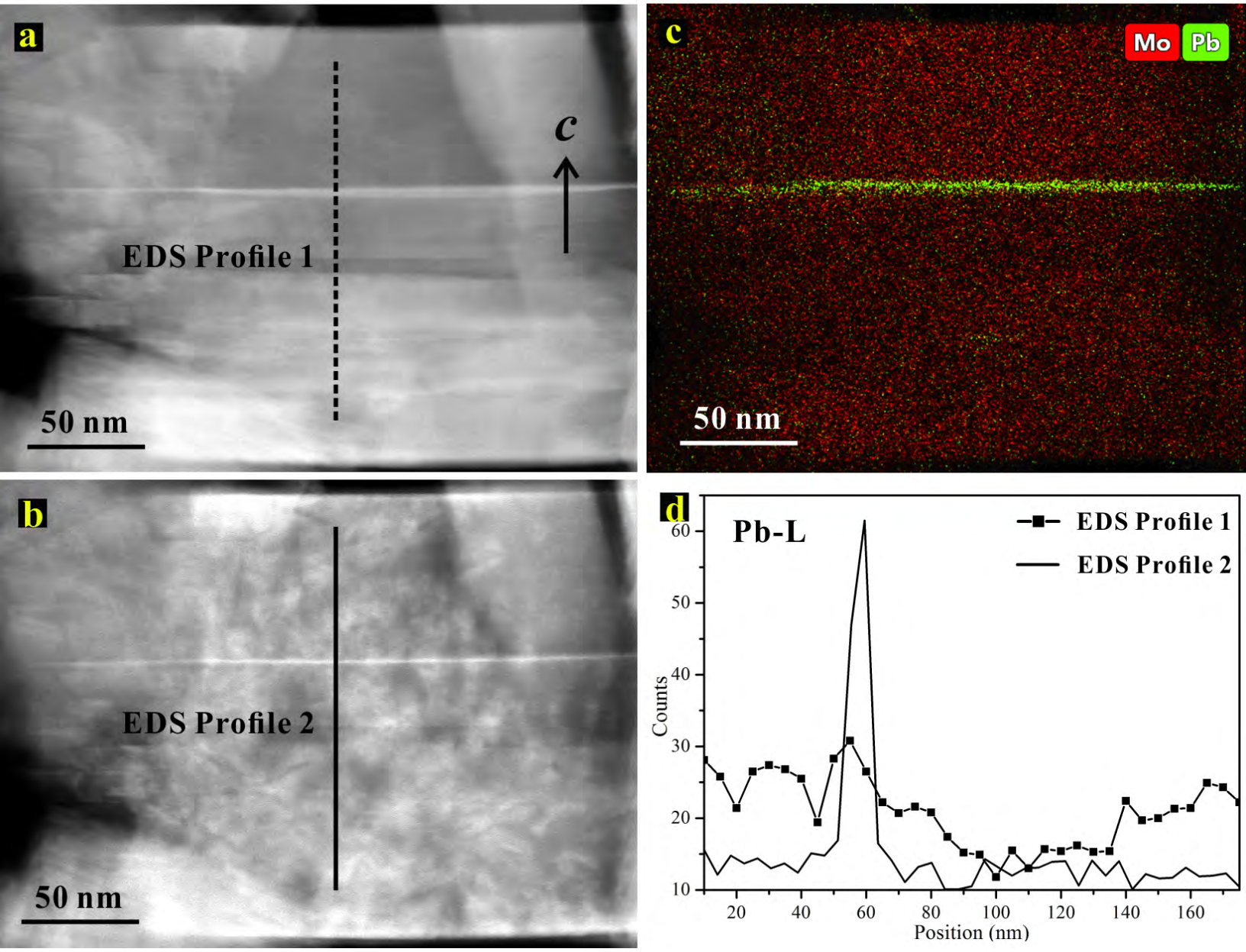
a
c
EDS Profile 1
50 nm
b
EDS Profile 2
50 nm
c
Mo
Pb
50 nm
d
Pb-L
EDS Profile 1
EDS Profile 2
Counts
Position (nm)
10
20
30
40
50
60
20
40
60
80
100
120
140
160

FIGURE 8

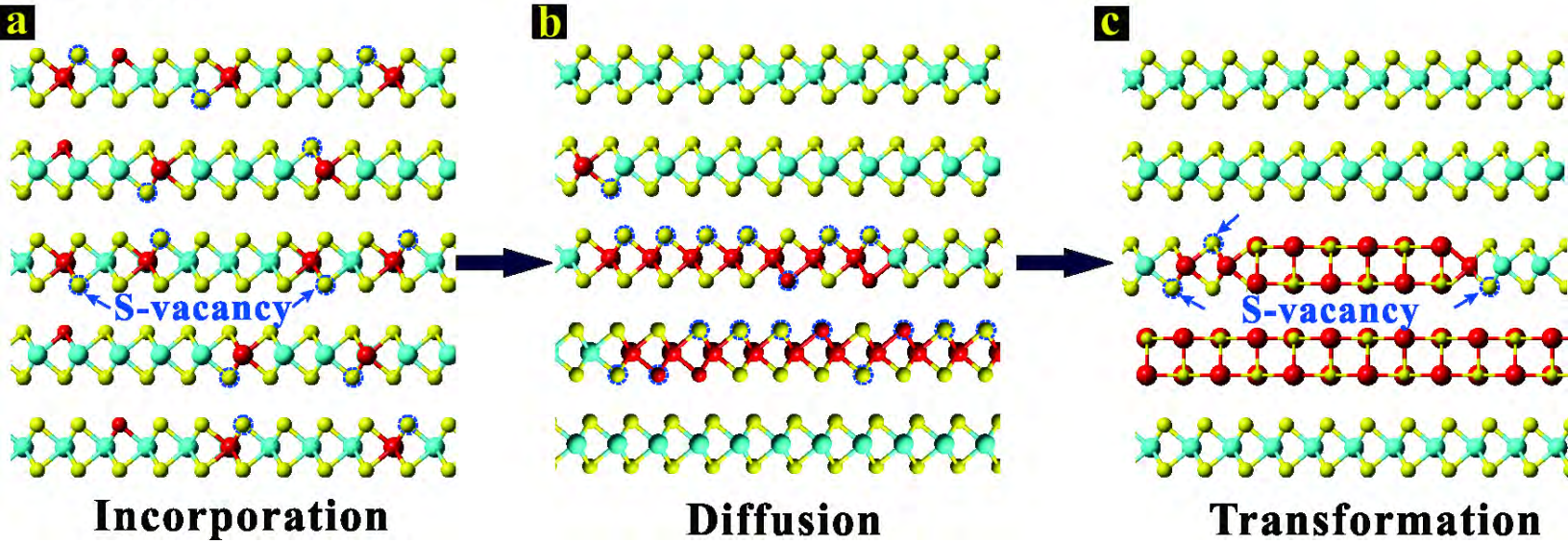
a
b
c
S-vacancy
S-vacancy
Incorporation
Diffusion
Transformation